JAAS

Accepted Manuscript

This is an *Accepted Manuscript*, which has been through the Royal Society of Chemistry peer review process and has been accepted for publication.

Accepted Manuscripts are published online shortly after acceptance, before technical editing, formatting and proof reading. Using this free service, authors can make their results available to the community, in citable form, before we publish the edited article. We will replace this *Accepted Manuscript* with the edited and formatted *Advance Article* as soon as it is available.

You can find more information about *Accepted Manuscripts* in the Information for Authors.

Please note that technical editing may introduce minor changes to the text and/or graphics, which may alter content. The journal's standard Terms & Conditions and the Ethical guidelines still apply. In no event shall the Royal Society of Chemistry be held responsible for any errors or omissions in this *Accepted Manuscript* or any consequences arising from the use of any information it contains.

ROYAL SOCIETY OF CHEMISTRY

www.rsc.org/jaas

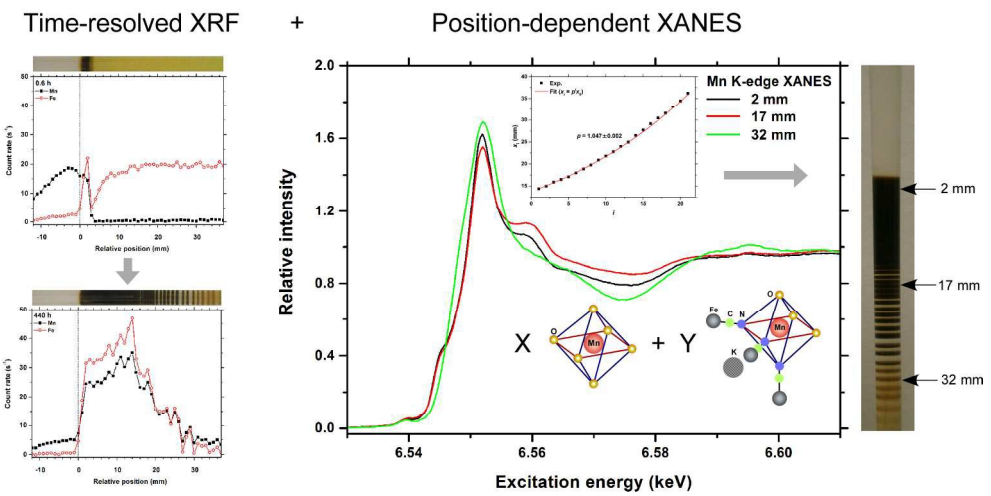

200x102mm (300 x 300 DPI)

Journal of Analytical Atomic Spectrometry

ARTICLE

X-ray Spectroscopic Analysis of Liesegang Pattern in Mn−Fe-Based Prussian Blue Analogs

Received 00th January 20xx,
Accepted 00th January 20xx

DOI: 10.1039/x0xx00000x

www.rsc.org/

Hisashi Hayashi*[a] and Hitoshi Abe[b,c]

We performed time-resolved X-ray fluorescence (XRF) and position-dependent X-ray absorption near-edge structure (XANES) measurements on gels containing Mn^{2+} and $[Fe(CN)_6]^{3-}$ ions. A sample tube containing an agar gel mixed with 0.20 M $MnCl_2$ solution and a water-glass gel mixed with 0.25 M $K_3[Fe(CN)_6]$ solution was prepared for these X-ray spectroscopic analyses. Periodic bands that obeyed the empirical scaling laws characteristic of Liesegang bands formed beyond the turbid zone in the water-glass gel. XRF results demonstrated that the turbid zone and the periodic bands contained diffusive Mn and Fe compounds. XANES results indicated that the Fe local structure in the sample tube was nearly independent of positions and was predominantly $[Fe(CN)_6]$. In contrast, the Mn local structure depended on position. FEFF calculations suggested that Mn−Fe-based Prussian blue analogs, of which the most likely local structure is $[Mn(NCFe)_3O_3K_3]$, co-existed with $[MnO_{6-n}Cl_n]$ (n = 0, 1) species and that their compositions were position-dependent.

Introduction

Processes in which chemical reactions are coupled with diffusion, *i.e.*, reaction-diffusion (RD) processes, have attracted much attention, because they have been observed in many forms in different natural systems and are essential in the functioning of biological systems.[1−15] In addition, Grzybowski *et al.*[12,16,17] recently developed experimental techniques for the initiation and control of RD processes in microgeometries. Their success has increased interest in RD processes in micro- and nanotechnology.

An important phenomenon in basic and applied studies of RD processes is periodic precipitation,[2−6,8,12,14−32] or Liesegang patterning.[33] Liesegang patterns form in gel media when one of the reagents, the inner electrolyte, is homogenized in the hydrogel, while the other, the outer electrolyte, interdiffuses in the gel. Two oppositely charged ions form less mobile precipitates (or aggregates) when their concentrations exceed the solubility product. Thus, due to the coupling of precipitation reaction(s) and diffusion, distinct precipitation bands may form periodically in the wake of a diffusive reaction front.[3,5,12,14,18,20,22,23] Nowadays, Liesegang patterning occurs in many scientific disciplines.[5,8,12,14,15] Furthermore, it is useful in microfabrication, because multiple structures can be generated in a simple way.[12,16,17]

Because RD processes and Liesegang patterning generally involve many elements,[12,16,24,26] the time dependence of the concentration distributions of each element and the chemical states of the locally formed, often amorphous, species[10,24,27,28,31] are indispensable pieces of information for their detailed studies. However, acquisition of these data using conventional techniques in previous studies of Liesegang patterning, such as light scattering,[2] FTIR,[31] XRD,[7,27,31] TEM,[8,13,31,32] SEM,[13,31] and UV-vis,[27,31] is difficult. Very recently, we proposed the combined use of two X-ray spectroscopic methods, *in situ* time-resolved X-ray fluorescence (XRF) spectroscopy and position-dependent X-ray absorption near-edge structure (XANES) spectroscopy, to study intricate RD processes in gels.[34] XRF[35−37] and XANES spectroscopy[35,38,39] are non-destructive and element-selective. They can be used to monitor *in situ* variations in elemental concentrations (XRF)[35,37] and the local microscopic structure of chemical species (XANES).[38,39]

Here, as an interesting extension of the previous study,[34] we have performed element-selective analyses of Liesegang patterns formed in gels containing Mn^{2+} and $[Fe(CN)_6]^{3-}$ ions by time-resolved XRF and position-dependent XANES spectroscopy. Mn^{2+} and $[Fe(CN)_6]^{3-}$ form Prussian blue analogs (PBAs),[40] which are cyano-bridged coordination polymers. PBAs have attracted attention, because of their diverse magnetic,[40] photomagnetic,[40−43] and electrochemical properties.[44−47] In particular, PBAs comprising Mn ions and $[Fe(CN)_6]$ ions (Mn−Fe-based PBAs) are intriguing as parent compounds for new photo-induced magnetic materials with high Curie temperatures ($Rb_xMn[Fe(CN)_6]_{(x+2)/3}\cdot yH_2O$)[41,42] and new cathode materials for advanced ion batteries ($Na_{1.76}Ni_{0.12}Mn_{0.88}[Fe(CN)_6]_{0.98}$[45] and $Ca_xNa_yMn[Fe(CN)_6]\cdot zH_2O$[47]). Although Liesegang patterning of PBAs has not been reported previously, it was evident in our experiments. The combination of periodic precipitation with

[a] *Department of Chemical and Biological Sciences, Faculty of Science, Japan Women's University, 2-8-1 Mejirodai, Bunkyo, Tokyo 112-8681, Japan. E-mail: hayashih@fc.jwu.ac.jp*
[b] *Institute of Materials Structure Science, High Energy Accelerator Research Organization, 1-1 Oho, Tsukuba, Ibaraki 305-0801, Japan.*
[c] *Department of Materials Structure Science, School of High Energy Accelerator Science, SOKENDAI (the Graduate University for Advanced Studies), 1-1 Oho, Tsukuba, Ibaraki 305-0801, Japan.*

wet stamping methods[12,16,17] has great potential as a simple, bottom-up approach to the fabrication of micro-battery and micro-(photo) magnetic arrays of PBAs.[48]

Experimental

Chemicals

Analytical reagent grade $K_4[Fe(CN)_6]\cdot 3H_2O$, $K_3[Fe(CN)_6]$, $CrCl_3\cdot 6H_2O$, $CoCl_2\cdot 6H_2O$, and $MnCl_2\cdot 4H_2O$ were obtained from Wako Pure Chemical Industries Ltd. (Chuo, Osaka) and were used without further purification. Acetic acid (1.00 M), agar powder (400–600 g/cm^2 gel strength), and sodium silicate solution (water-glass, 52–57% assay, 2.06–2.31 SiO_2/Na_2O mole ratio) were also acquired from Wako Pure Chemical Industries Ltd. All aqueous solutions were prepared using deionized water.

Tube preparation

Quartz glass tubes containing the inner and outer electrolyte gels were prepared as follows. For the inner electrolyte ($[Fe(CN)_6]^{3-}$ or $[Fe(CN)_6]^{4-}$), water-glass (1.6 g) was dissolved in deionized water (10 mL). Appropriate amounts of $K_3[Fe(CN)_6]$ or $K_4[Fe(CN)_6]\cdot 3H_2O$ were added to deionized water (5 mL) to prepare 0.10–0.30 M $[Fe(CN)_6]^{3-}$ or $[Fe(CN)_6]^{4-}$ solutions. The two solutions were mixed, and acetic acid (16 mL, 0.53 M) was added. The water-glass sol was stirred continuously for 5 min to allow homogenization, and transferred to quartz glass tubes 80 mm long, 4.0 mm in inner diameter, and 0.010 mm thick (Mark-tube, Hilgenberg GmbH, Malsfeld) using a Pasteur pipette. The sol solidified to a gel within 10 min.

For the outer electrolyte (Mn^{2+}, Cr^{3+}, or Co^{2+}), a 2% (w/w) agar sol was prepared by adding agar powder to deionized water (20 mL). The appropriate amount of $MnCl_2\cdot 4H_2O$, $CrCl_3\cdot 6H_2O$, or $CoCl_2\cdot 6H_2O$ was added to the suspension to yield metal ion concentrations of 0.10 to 0.30 M. The mixture was heated at ~80 °C with continuous stirring until the agar dissolved (a few minutes). The resulting hot sol was immediately poured over the solidified water-glass gel in the quartz glass tubes using a Pasteur pipette, and the tubes were covered with Parafilm. The agar sol solidified to a gel within 5 min. We used the tube prepared from 0.20 M Mn^{2+} and 0.25 M $[Fe(CN)_6]^{3-}$ solutions, hereafter identified as the "sample tube," for X-ray measurements. The tube was mounted on a handmade holder [acrylic resin; 80 × 30 × 10 mm ($h \times w \times d$)], the height and width of which were graduated in mm, to identify band positions in the gels and to facilitate transitions between band monitoring and XRF/XANES measurements.

Monitoring the evolution of colored bands in the gel

After addition of the sol to the water-glass gel, the electrolyte components in both media diffuse and react with one another. Colored bands form near the junction, as shown in Figs. 1 and 2. The evolution of the bands at room temperature (~20 °C) was recorded for up to 30 days using a digital camera with intermittent *in situ* XRF measurements performed on the sample tube. Mn and Fe *K*-edge XANES spectra of fully developed bands (*i.e.*, those exhibiting no further changes with time) in the sample tube were also measured. The sample tube was fully developed after ~400 h.

Laboratory *in situ* time-resolved XRF measurements

Details of the *in situ* laboratory XRF measurements have been described.[34] Briefly, an 18-kW X-ray generator (Rigaku, RU-300) with a Cu target operated at 200 mA and 40 kV was used for excitation. Cu $K\alpha_1$ X-rays from the generator were selected and focused to within ~0.5 mm in the horizontal direction by a SiO_2 $(10\bar{1}1)$ Johansson-type crystal monochromator.[49] Divergence of X-rays in the vertical direction was limited by a handmade collimator with a ~0.5 mm slit. The sample tube in its holder was placed on a computer-controlled *X-Z* stage (Kohzu Precision, XA05A-L2) and moved in 1-mm steps in the *Z* direction. The XRF signal at each position was detected using a silicon drift detector (Amptek, XR-100T). The XRF signals were collected for 100 s at each point by a multichannel analyzer (MCA, Amptek, MCA8000A). The time required for collection of a complete XRF distribution over ~50 mm of the sample tube was ~1.4 h. As shown in ref. 49, the counts for the XRF peaks (here, Mn Kα and Fe Kα peaks) and the background components of the spectra were integrated over 20 channels in the MCA (0.39 keV energy width). After subtracting the background from the raw Mn and Fe signals, the resulting intensities were used to construct the Mn Kα and Fe Kα distributions in the sample tube.

Position-dependent XANES measurements using synchrotron radiation

Details of the position-dependent XANES measurements also have been described.[34] XANES spectra at the Mn and Fe *K*-edges were collected at the bending-magnet beamline BL-9C of KEK-PF, High Energy Accelerator Research Organization, Tsukuba, Japan. The storage ring was operated at 2.5 GeV with a 450 mA current. A Si(111) double-crystal monochromator was used to produce monochromatic X-rays, the energy resolution of which was ~1.4 eV. The beam size at the sample position was 1.0 × 1.0 mm ($h \times w$).

The sample tube in its holder was placed on a computer-controlled *Z* stage (Chuo Precision Industrial, ALV-102-HP). XANES spectra at the Mn and Fe *K*-edges were collected at room temperature at 6.450−6.750 and 7.000−7.300 keV, respectively. Measurements were carried out in the fluorescence mode by placing a Lytle-type detector normal to the beam. Fluorescence signals were collected for 5–10 s at each incident energy. The typical accumulation time of a spectrum was ~1 h. Mn and Fe *K*-edge XANES spectra of $K_3[Fe(CN)_6]$, $K_4[Fe(CN)_6]\cdot 3H_2O$, and $MnCl_2\cdot 4H_2O$ were obtained for comparison. The measurements of these standard samples were carried out in transmission mode using an ion chamber as detector.

After approximating the profiles observed at 6.450−6.520 keV (the region before the Mn pre-edge) and 7.000−7.100 keV (the region before the Fe pre-edge) as straight lines and subtracting this background component, the XANES spectra obtained were normalized by assuming that the average

absorption coefficients for Mn and Fe are the same at energies of 6.700−6.750 keV (for Mn) and 7.250−7.300 keV (for Fe). Normalized XANES data were used to examine the chemical states of Mn and Fe species in the gels. To simulate the observed XANES spectra, *ab initio* self-consistent real-space multiple scattering calculations were carried out using the FEFF 8.02 code.[50,51]

Results and discussion

Macroscopic observations of Liesegang patterns in gels containing Mn^{2+} and $[Fe(CN)_6]^{3-}$

Preliminary experiments with tube preparations prior to X-ray measurements indicated that periodic brown bands form in water-glass gels, prepared with 0.15−0.30 M $[Fe(CN)_6]^{3-}$ solutions and contacted by agar gels containing 0.15−0.30 M $MnCl_2$. For example, Fig. 1(a)−(d) shows the patterns formed in gels prepared with (a) 0.10, (b) 0.15, (c) 0.25, and (d) 0.30 M $[Fe(CN)_6]^{3-}$ solutions and a 0.20 M $MnCl_2$ solution. Distinct periodic bands were observed in gels prepared with concentrated $[Fe(CN)_6]^{3-}$ [Fig. 1(c) and (d)]. In contrast, at low (<0.10 M) concentrations, only a diffusive, broad band was observed [Fig. 1(a)].

The pattern obtained depended on the Fe oxidation state. With $[Fe(CN)_6]^{4-}$ as inner electrolyte, no periodic pattern was observed at any concentration. For example, only a white band was observed near the gel junction in Fig. 1(e), where the concentrations of the Mn^{2+} and $[Fe(CN)_6]^{4-}$ solutions were 0.20 and 0.25 M, respectively.

Periodic pattern formation is not a general property of PBA systems. For example, no clear periodic pattern was observed when using Cr^{3+} and Co^{2+} in place of Mn^{2+}. Fig. 1(f) and (g) show the absence of discrete bands in tubes prepared from 0.20 M Cr^{3+} solution and 0.25 M $[Fe(CN)_6]^{3-}$ or $[Fe(CN)_6]^{4-}$ solutions. Fig. 1(h) and (i) show that 0.20 M Co^{2+} solution also produced no clear periodic patterns in water-glass gels prepared with 0.25 M $[Fe(CN)_6]^{3-}$ or $[Fe(CN)_6]^{4-}$ solutions.

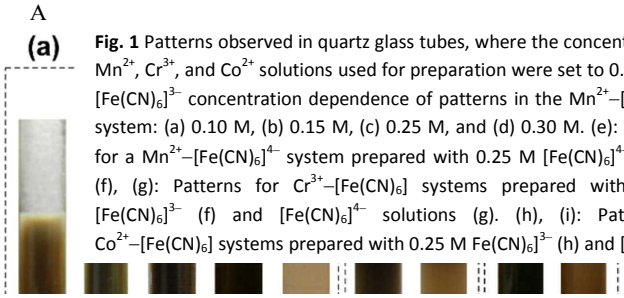

Fig. 1 Patterns observed in quartz glass tubes, where the concentrations of Mn^{2+}, Cr^{3+}, and Co^{2+} solutions used for preparation were set to 0.20 M. The $[Fe(CN)_6]^{3-}$ concentration dependence of patterns in the Mn^{2+}–$[Fe(CN)_6]^{3-}$ system: (a) 0.10 M, (b) 0.15 M, (c) 0.25 M, and (d) 0.30 M. (e): The result for a Mn^{2+}–$[Fe(CN)_6]^{4-}$ system prepared with 0.25 M $[Fe(CN)_6]^{4-}$ solution. (f), (g): Patterns for Cr^{3+}–$[Fe(CN)_6]$ systems prepared with 0.25 M $[Fe(CN)_6]^{3-}$ (f) and $[Fe(CN)_6]^{4-}$ solutions (g). (h), (i): Patterns for Co^{2+}–$[Fe(CN)_6]$ systems prepared with 0.25 M $Fe(CN)_6]^{3-}$ (h) and $[Fe(CN)_6]^{4-}$

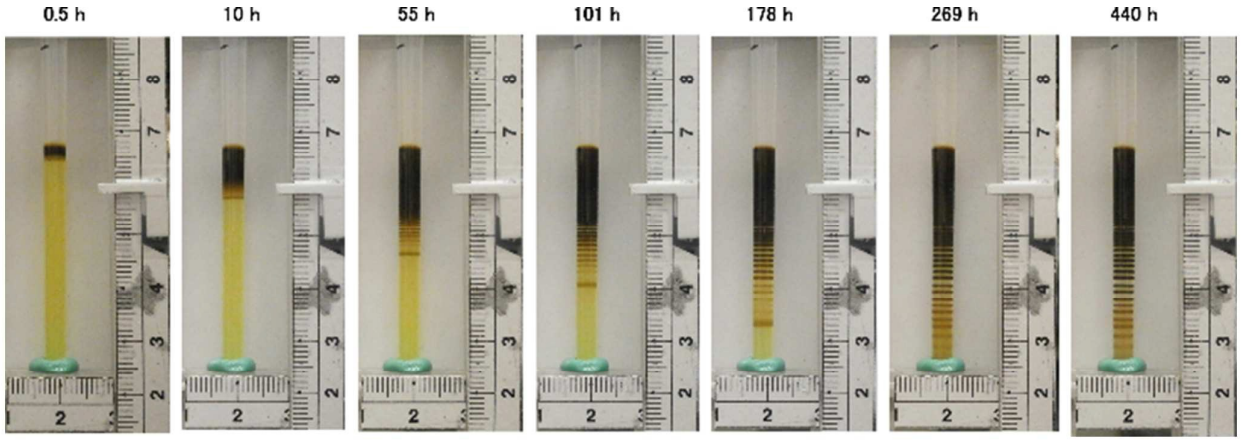

Fig. 2 Spatiotemporal evolution of brown bands in the sample tube in its holder. Elapsed time after addition of the agar sol is indicated at the top of each picture.

n important factor accounting for the trends in Fig. 1 is the solubility of the PBAs. As shown in a recent simulation study,[52] little or no precipitation occurs and periodic band formation is not observed, if the solubility of reaction products is very high (the Cr^{3+} case). However, if the solubility of reaction products is very low (the Co^{2+} case), closely spaced or continuous precipitation occurs. The products in the Mn^{2+}–$[Fe(CN)_6]^{3-}$ system have intermediate solubility and are well-suited to periodic precipitation.

Based on these observations, we determined the concentrations for preparing the sample tube as 0.20 M for the Mn^{2+} solution and 0.25 M for the $[Fe(CN)_6]^{3-}$ solution. As shown in Fig. 1(c), these concentrations produced the clearest periodicity over a large distance.

Fig. 2 shows the spatiotemporal evolution of the brown bands formed of the sample tube. The agar gel in the upper part of sample tube remained almost colorless over a period of 30 days. In contrast, changes were observed in the yellow water-glass gel in the lower part of the tube. Initially, a brown band formed near the gel junction and propagated downwards through the tube. After ~5 h, when the band had propagated to a distance of ~7 mm from the junction, it split and produced a new, relatively narrow band at the reaction front. Separation of the band at the reaction front became clear after ~10 h. The reaction front continued to move downwards for up to ~200 h after the addition of Mn^{2+} leaving behind narrow, periodic brown bands. These bands also moved downwards with time unlike the multicolored bands formed in the Fe^{3+}–$[Fe(CN)_6]^{3-}$ system.[34] The diffusive movement of the brown bands became less noticeable after ~200 h and effectively stopped after ~350 h. The photograph taken at 440 h shows the fully developed bands in the sample tube.

It is well known that Liesegang patterns obey a common set of empirical scaling laws irrespective of the electrolyte pair and geometry of the system. These are known as the spacing law, the width law, and the time law.[5,12,14,15,22,52] Consider that precipitation bands with widths of w_1, w_2, w_3,…, w_n are formed at locations x_1, x_2, x_3,…, x_n measured from the gel junction, and that the time elapsed until the formation on the i-th (i = 1,2,3,…,n) band is t_i. The spacing law states that the ratio x_{i+1}/x_i is constant for all bands, and that the positions of the bands form a power series, $x_i = p^i x_0$. $p = x_{i+1}/x_i$ is the spacing coefficient and for most systems is larger than 1, but does not exceed 1.5. The width law states that the ratio of the widths of two consecutive bands, w_{i+1}/w_i, is constant (q_1). The widths of the bands also form a power series, $w_i = q_1^i w_0$. The time law states that the value of x_i^2/t_i approaches a constant (q_2) as i increases. In other words, $x_i \approx q_2\sqrt{t_i}$ for large i. The time law is quantitatively similar to the definition of the diffusion coefficient, which is a direct consequence of the diffusive transport of precipitates in the gel.[12]

To determine whether the brown bands observed in the sample tube obey these scaling laws, the interband spacing and bandwidths were measured using the millimeter graduations on the sample holder with a precision of ± 0.1 mm.

Fig. 3(a) shows the plot of band locations (x_i) versus band number (i) for the fully developed pattern at 564 h. Curve fitting by the function $x_i = p^i x_0$ is also shown. All band positions were well reproduced by the function $x_i = 1.047^i \times x_0$. The spacing coefficient of 1.047 ± 0.002 is typical of systems producing Liesegang patterns.[12,14,16]

Fig. 3(b) shows the band widths (w_i) versus band number (i) for the fully developed pattern. Curve fitting with the function $w_i = q_1^i w_0$ is also shown. Because many brown bands were narrower than the millimeter graduations employed, the experimental uncertainty in w_i was relatively large. Although this resulted in considerable data scatter, the general trend of increasing band width with increasing i was reproduced by the function $w_i = 1.021^i \times w_0$. Although the data points in Fig. 3(b) appear to "oscillate" around the fitting function, no theory is available to explain such behavior. This interesting aspect is open to more accurate investigation in the future.

All 21 bands in the sample tube obeyed the time law. As an example, Fig. 3(c) shows the location (x_i) of several bands (i = 8, 10, 12, 14) and of the reaction front versus the square root of time ($t^{0.5}$). Fits by the function $x_i = q_2\sqrt{t_i} + x_{i0}$ are also shown. The positions of each band is described by the function $x_i \propto q_2\sqrt{t_i}$. Values of q_2 for the reaction front and the 14th, 12th, 10th, and 8th bands were 2.28 ± 0.03, 1.87 ± 0.03, 1.73 ± 0.03, 1.56 ± 0.04, and 1.40 ± 0.04 mm/h$^{0.5}$, respectively. The value of the slope (q_2) increases with increasing i (or the relative distance of each band from the gel junction). This trend is common in

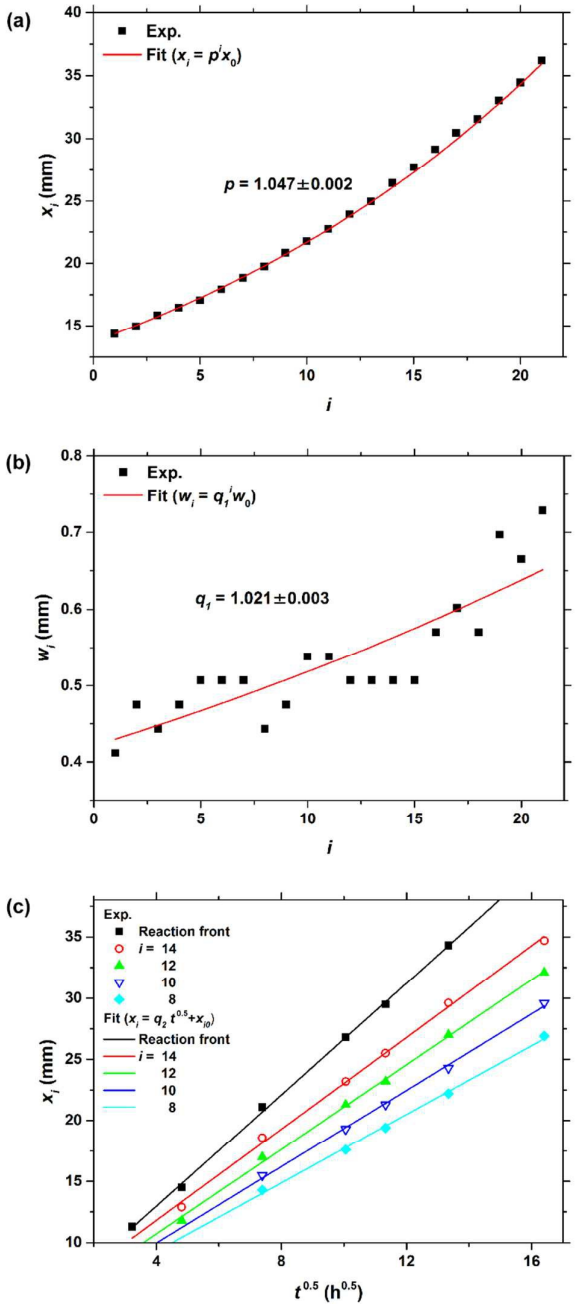

Fig. 3 (a) Band locations (x_i) and (b) band widths (w_i) versus band number, i, for the fully developed pattern in the sample tube at 564 h. In (a) and (b), the curves were fitted using the functions $x_i = p^i x_0$ and $w_i = q_1^i w_0$, respectively. (c) Band locations (x_i) of several bands (i = 8, 10, 12, 14) and of the reaction front versus the square root of time ($t^{0.5}$). Fitting lines described by the function $x_i = q_2\sqrt{t_i} + x_{i0}$ are also shown.

systems forming Liesegang patterns.[21]

Thus, Fig. 3 clearly shows that the patterns observed in the sample tube satisfy the scaling laws of Liesegang patterns, which suggests that the patterns arise from a mechanism producing normal Liesegang patterns.

The model of Chacron and L'Heureux[23] is helpful in understanding the mechanism of Liesegang pattern formation. Consider the simple ionic reaction $aA^{s+} + bB^{t-} \rightarrow C$ in the tube containing the gel. Here, A^{s+}, B^{t-}, and C correspond to the aquomanganese(II) ion, $[Fe(CN)_6]^{3-}$, and the PBA, respectively. The electrolytes A^{s+} and B^{t-} diffuse through the gel and rapidly form compound C when the product of their concentrations exceeds the solubility product. Chacron and L'Heureux describe Liesegang patterning as the interplay among the processes of diffusion, nucleation, growth, and ripening. When nucleation and growth kinetics are dominant, supersaturation of species C triggers its nucleation and crystallization to form a precipitation band. No further nucleation occurs at the band location due to depletion of reactants in the immediately surrounding area. As a result, the reaction zone moves down the tube. When C again achieves its supersaturation level at the moving reaction front, the next precipitation band forms and these events are repeated. This description is the so-called pre-nucleation model.[5,12,14,18,20]

In contrast, when nucleation rapidly ceases and subsequent ripening becomes important, the growth of larger particles by aggregation of smaller ones is favored, because larger particles have lower surface energy. The larger particles form a precipitation band, which evolves through ripening after nucleation has ceased. Consequently, the reactant concentrations decrease in the vicinity of the band and cause the reaction zone to move downwards. Periodic precipitation occurs by this process. Models based on these particle-growth and ripening effects are called post-nucleation models.[1,5,12,14,19]

In general, pre-nucleation models generate periodic precipitation that satisfies the scaling laws,[12,52] but cannot describe the formation of secondary precipitation bands between two major bands that is observed in some RD systems (*e.g.* the Mg^{2+}–OH^- system[1,2]). Post-nucleation models can account for such secondary band effects, but rigorous theory including quantitative relationships between particle growth and particle size is lacking.[52]

The agreement with the scaling laws (Fig. 3) and lack of evident secondary bands (Figs. 1 and 2) strongly suggest that nucleation and growth kinetics were dominant in the sample tube. In other words, pre-nucleation models provide a suitable basis for explaining the mechanism of the observed pattern formation.

The main difference between the current system and other systems showing Liesegang patterns[5,12,14] is that the chemical species participating in band formation are not well characterized. Firstly, product C, which is Mn–Fe-based PBA, is polymeric and has no well-defined structure. Thus, these PBAs may be amorphous, poorly crystalline, or composed of several phases.[40] Secondly, the water content of PBAs may vary as a function of chemical environment, and linkage isomerism via bridging cyanide ligands and intermetallic charge transfer or redox processes may occur.[40] Thirdly, PBAs can intercalate a wide range of ions,[40–43,45–48] including K^+, which makes their structures more complicated. Fourthly, reactant ion A^{s+}, which is an aquomanganese(II) ion in $MnCl_2$ solutions is in equilibrium with complex ions of the series $[MnCl_{(6-j)}(H_2O)_j]^{(j-4)+}$.[53,54] Fifthly, reactant ion B^{t-}, $[Fe(CN)_6]^{3-}$, can be hydrolyzed or reduced before reacting with the A^{s+} ions.[40] X-ray spectroscopic results are presented and discussed in the following sections to shed light on these complicated, poorly-understood chemical species producing Liesegang patterns.

Time-resolved XRF intensity distributions

Fig. 4 shows examples of the XRF spectra obtained from the outer electrolyte (Mn^{2+}) dominant region (3 mm above the gel junction: $X = -3$ mm) at 0.6 h after addition of the agar sol (t = 0.6 h, black squares), the inner electrolyte ($[Fe(CN)_6]^{3-}$) dominant region (X = 37 mm, t = 0.6 h, red circles), and the mixing region (X = 12 mm, t = 440 h, green triangles). In general, the background profiles of the XRF spectra overlapped within experimental error confirming the high stability of the incident X-ray beams during intensity distribution measurements.

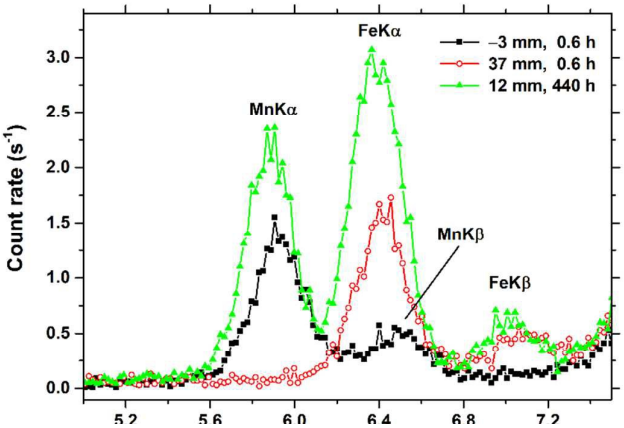

Fig. 4 XRF spectra obtained from the outer electrolyte (Mn^{2+}) dominant region (3 mm above the gel junction at 0.6 h after addition of the agar sol; black squares), the inner electrolyte ($[Fe(CN)_6]^{3-}$) dominant region (37 mm below the gel junction at 0.6 h after sol addition; red circles), and the mixing region (12 mm below the gel junction at 440 h after sol addition; green triangles).

In the outer and inner electrolyte dominant regions, Mn Kα and Kβ and Fe Kα and Kβ lines were clearly observed. Mn Kα and Fe Kα signals were used to establish Mn and Fe XRF intensity distribution profiles. As shown in Fig. 4, the energy of the Fe Kα and Mn Kβ lines completely overlapped resulting in observation of three, not four, XRF peaks in the mixing region. Because of this overlap, Fe Kα intensity distributions were determined after subtraction of the estimated Mn Kβ contribution. The Mn Kβ ($K\beta_1 + K\beta_{2,5}$) intensity was estimated to be 11.8% of the Mn Kα ($K\alpha_1 + K\alpha_2$) intensity.[55]

Note that the Fe Kβ (~7.1 keV) intensity at 12 mm (green) is comparable to that at 37 mm (red), whereas the Fe Kα (~6.4

keV) intensity at 12 mm is about twice that at 37 mm. This is due to secondary absorption[56] by Mn (~6.5 keV *K*-edge energy). It is well-known[56] that secondary Mn absorption can enhance Mn XRF. Thus, Fig. 4 suggests that the Mn Kα intensity distributions in Fig. 5 may be slightly enhanced (< ~10%) in the mixing region.

Fig. 5 shows the time dependence of the Mn Kα and Fe Kα intensity distributions in the sample tube. Examination of Fig. 5 reveals that the integrated areas, particularly that of Mn Kα, increase with time. These signal increments arise primarily from the regions *not* illustrated by the snapshots in Fig. 5, which include an additional ~10 mm of agar gel containing Mn

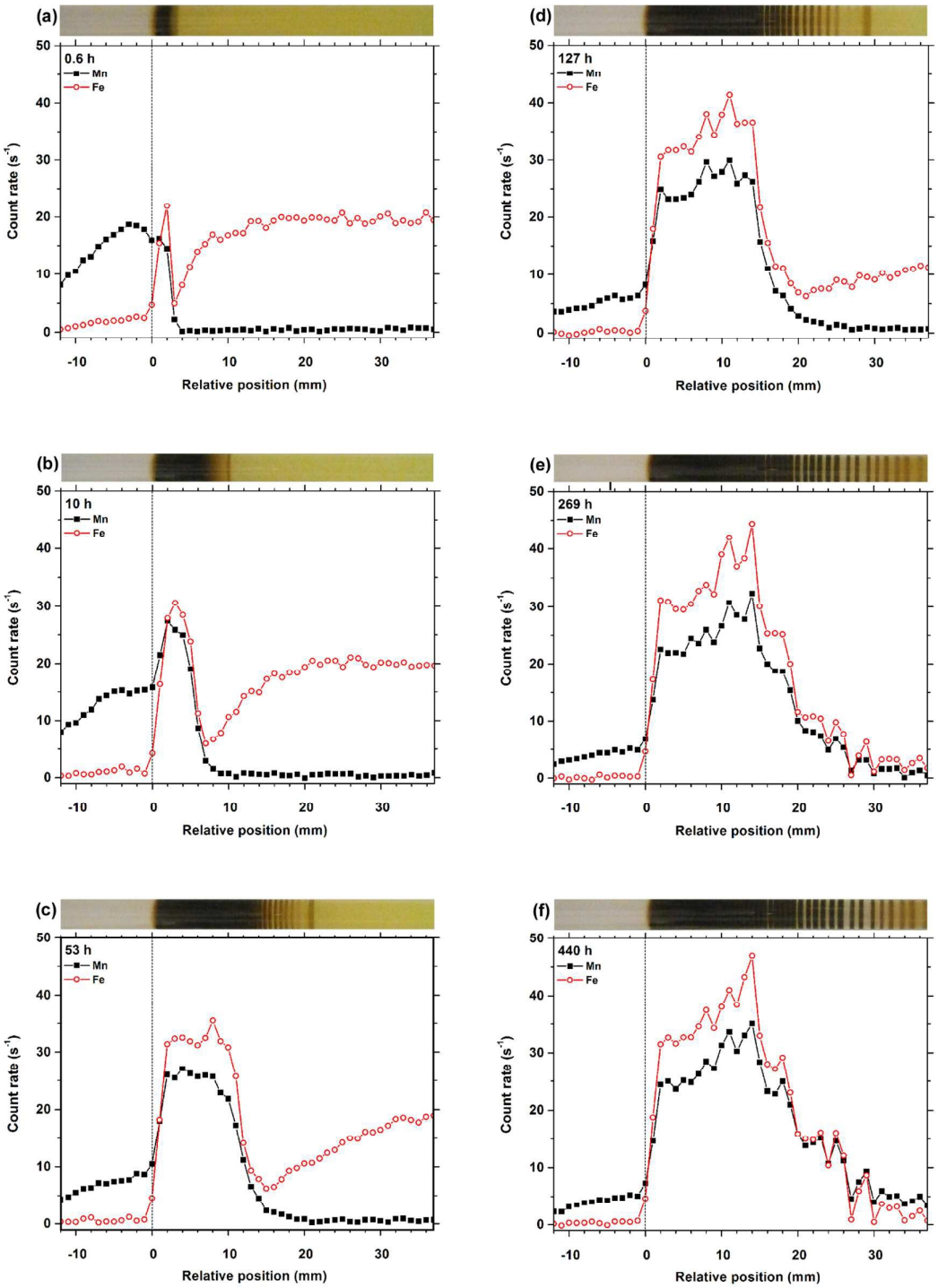

Fig. 5 Mn Kα and Fe Kα intensity distributions in the sample tube measured at (a) 0.6, (b) 10, (c) 53, (d) 127, (e) 269, and (f) 440 h after addition of the outer electrolyte. Snapshots at each measurement time are displayed at the top of the figures to facilitate comparison of the XRF distributions with the positions of the brown bands.

on the left and ~5 mm of water-glass gel containing Fe on the right.

Although the effects of Mn enhancement need to be considered, the XRF distributions in Fig. 5 provide a good approximation of the concentration distributions of each element in the gels and precipitates. In studies of Liesegang patterns, the distributions in gels (containing reactant electrolytes) and precipitates (forming periodic bands) have been important in pre-nucleation theories[5,18] and experiments on multi-component (*e.g.*, $Mg(OH)_2$+$VO(OH)_2$[52]) systems, respectively. The XRF results in Fig. 5 were obtained at varying times after addition of the outer electrolyte, as indicated with each intensity distribution. The vertical and horizontal axes in Fig. 5 are the count rate of the XRF signals and the distance from the gel junction (X), respectively. To facilitate comparison of the XRF intensity distributions with the positions of the brown bands, the snapshots obtained at each time are displayed at the top of Fig. 5(a)–(f).

The Mn Kα and Fe Kα intensity distributions changed significantly with time in accordance with the macroscopic evolution of the brown bands. Shortly after initiation [0.6 h, Fig. 5(a)], the Mn Kα distribution established a threshold below the gel junction (X = 3 mm, corresponding to the position of the boundary of the short brown band) indicating that Mn species had diffused into the water-glass gel. In the brown area ($0 \leq X \leq 3$ mm), the Fe Kα distribution showed a clear peak followed by a deep valley at X = 3 to 8 mm. This observation suggests that Fe species ($[Fe(CN)_6]^{3-}$) moved from the valley region to the brown band region to form Mn−Fe-based PBAs.

At ~10 h after Mn^{2+} addition, a peak was observed in the Mn Kα distribution below the junction ($X \approx 3$ mm) that almost overlapped the peak in the Fe Kα distribution [Fig. 5(b)]. Unlike the Fe^{3+}–$[Fe(CN)_6]^{3-}$ system studied previously,[34] the increase in peak intensities with time was not very significant near the gel junction. Instead, the thresholds of these peaks, which correspond to the edge of the broad, turbid zone, continued to shift downward to $X \approx 14$ mm [Fig. 5(c)] at times up to ~60 h. These shifts indicate significant diffusion of the PBA products, which are not fixed near the gel junction, to the bottom of the sample tube.

Although the shift of the main distribution peaks to greater X effectively stopped after ~60 h, the reaction front still moved downward with Liesegang bands appearing behind the frontal band (see Fig. 2). In accordance with these observations, the XRF distribution profiles at $X \geq 16$ mm showed considerable changes up to ~250 h [Fig. 5(c), (d), and (e)].

At this intermediate stage, the Fe Kα intensity was much greater than the Mn Kα intensity at large X suggesting the presence of large quantities of unreacted Fe species in the lower part of the sample tube. As time progressed, the Fe Kα intensities became weaker and were almost equaled by the corresponding Mn Kα intensities. Meanwhile, the shapes of the Mn Kα and Fe Kα distribution peaks became more distinct at locations agreeing approximately with the position of the Liesegang bands. These results suggest that unreacted Fe species were consumed in the production of Mn−Fe-based PBAs, which resulted in the formation of a clearer Liesegang pattern.

After ~250 h, the Mn Kα and Fe Kα distributions showed very little time-dependent change [compare Fig. 5(e) and (f)] in accordance with the visual observations. The XRF intensities of the distinct peaks (periodic bands) were typically 1/3–1/6 those of the broad main peaks (turbid zone). These findings suggest that the PBA concentrations in the turbid zone were much greater than those in the periodic bands, although this was less noticeable to the naked eye.

Fig. 6 (a) Fe *K*-edge XANES spectra of the sample tube, $K_4[Fe(CN)_6]\cdot 3H_2O$, and $K_3[Fe(CN)_6]$ and the positions in the sample tube at which the Fe *K*-edge XANES spectra were measured. (b) Mn *K*-edge XANES spectra of the sample tube and $MnCl_2\cdot 4H_2O$ and the positions in the sample tube at which the Mn *K*-edge XANES spectra were measured. The sampling positions are indicated by arrows on the snapshots at the right-hand side of each figure. The snapshots were taken at 564 h. The labels "T" and "F" indicate transmission and fluorescence mode measurements,

The XRF results can be summarized as follows: (1) the broad, main band (the turbid zone) contained diffusive Mn and Fe compounds gathered from the surroundings; (2) the narrow, discrete bands formed at low concentrations of Mn and/or Fe species co-existed with large amounts of unreacted Fe species during intermediate stages and became distinct in the lower region at the fully developed stage; and (3) the concentrations of Mn and Fe species in the turbid zone were 3–6 times greater than those in the periodic bands. These findings strongly support the idea that Mn−Fe-based PBAs were produced and contributed to the formation of the Liesegang pattern.

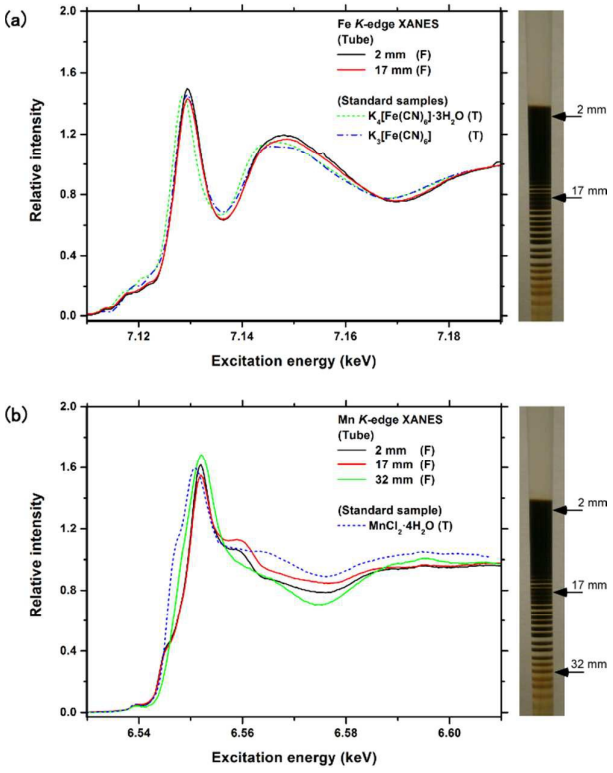

Position-dependent XANES spectra

The Fe and Mn *K*-edge XANES spectra of the sample tube shown in Fig. 6(a) and (b), respectively, were obtained in the fluorescence mode (denoted as "F"), because the sample was too thick (4.0 mm) to use the transmission ("T") mode. The measured fluorescence intensities of Fe and Mn were less than 10% of those of standard samples ($K_3[Fe(CN)_6]$, $K_4[Fe(CN)_6]\cdot 3H_2O$, and $MnCl_2\cdot 4H_2O$) even at the white line energy. Observation of weak intensities suggests that the concentrations of Fe and Mn in the sample tube were low enough to avoid self-absorption effects in fluorescence mode XANES, as was estimated in ref. 34. This assumption is supported by the good agreements in the Fe *K*-edge XANES profile between the sample tube (F) and the standard hexacyanoferrate compounds (T) in Fig. 6(a).

Fe *K*-edge XANES was measured at two sampling positions labeled as "2 mm" (2 mm below the gel junction in the turbid zone) and "17 mm" (17 mm below the gel junction among the dense periodic bands). Unfortunately, limited time on the beamline prevented us from collecting Fe XANES data at "32 mm", where Mn *K*-edge data were obtained. The positions of the measurements are indicated by arrows in the snapshots on the right-hand side of the figure. For comparison, Fe *K*-edge XANES spectra of $K_4[Fe(CN)_6]\cdot 3H_2O$ and $K_3[Fe(CN)_6]$ obtained in transmission mode are also plotted in Fig. 6(a). These XANES profiles agree well with those in ref. 57. The XANES profiles of $K_3[Fe(CN)_6]$ and $K_4[Fe(CN)_6]\cdot 3H_2O$, where Fe^{3+} and Fe^{2+} ions have strong bonds with six CN^- ions in O_h symmetry, are similar. This reflects the strong similarity of their local atomic structures.

As evident from Fig. 6(a), the Fe *K*-edge XANES spectra obtained in the sample tube were almost identical and agreed qualitatively with the hexacyanoferrate spectra. Besides the negligible self-absorption effects mentioned above, these findings indicate even in the highly mixed turbid zone and periodic band regions that (1) the local structure around Fe atoms in the sample tube was almost the same at all measured positions, and (2) the Fe atoms were primarily surrounded by CN^- in octahedral geometry. These results are consistent with the well-known fact that the $[Fe(CN)_6]$ moiety has considerable stability and generally retains its structure in aqueous solutions and gels.

Fig. 6(b) shows the Mn *K*-edge XANES spectra of the sample tube measured at three positions labeled "2 mm" (turbid zone), "17 mm" (dense periodic bands), and "32 mm" (sparse periodic bands). These positions are indicated by arrows in the snapshots on the right-hand side of the figure.

In contrast to the Fe XANES results, the Mn XANES spectra depended distinctly on the measuring position, although the brown color at each position appeared to be similar. Although the overall XANES profile at 2 mm agrees fairly well with that at 17 mm, there are significant differences in the relative intensities of the second peak at ~6.56 keV and the following shallow valleys. The differences in the XANES profile at 32 mm are more pronounced, where the 6.56 keV peak is missing, the valley depth is deeper, and the position of the *K*-edge shifts to lower energy. These findings mean that the local structures and symmetries around Mn are considerably position dependent.

For comparison, the Mn *K*-edge XANES spectrum of $MnCl_2\cdot 4H_2O$ obtained in the transmission mode is also presented in Fig. 6(b). The XANES profile observed agrees well with those in refs. 58 and 59. Here, the Mn^{2+} ions in crystalline $MnCl_2\cdot 4H_2O$ are present as the *cis*–$[MnCl_2(H_2O)_4]$ complex.[53,54] The differences in Mn XANES spectra between $MnCl_2\cdot 4H_2O$ and the sample tube are large. For example, in $MnCl_2\cdot 4H_2O$ the white line energy is shifted to the lower energy with a shoulder at 6.547 keV, a plateau exists from 6.557 to 6.566 keV, and the relative intensity of the valley at ~6.576 keV is greater. These differences suggest that $MnCl_2(H_2O)_4$ complexes are not necessarily dominant in the sample tube, which would be expected if the Mn−Fe-based PBAs occur at the measured positions.

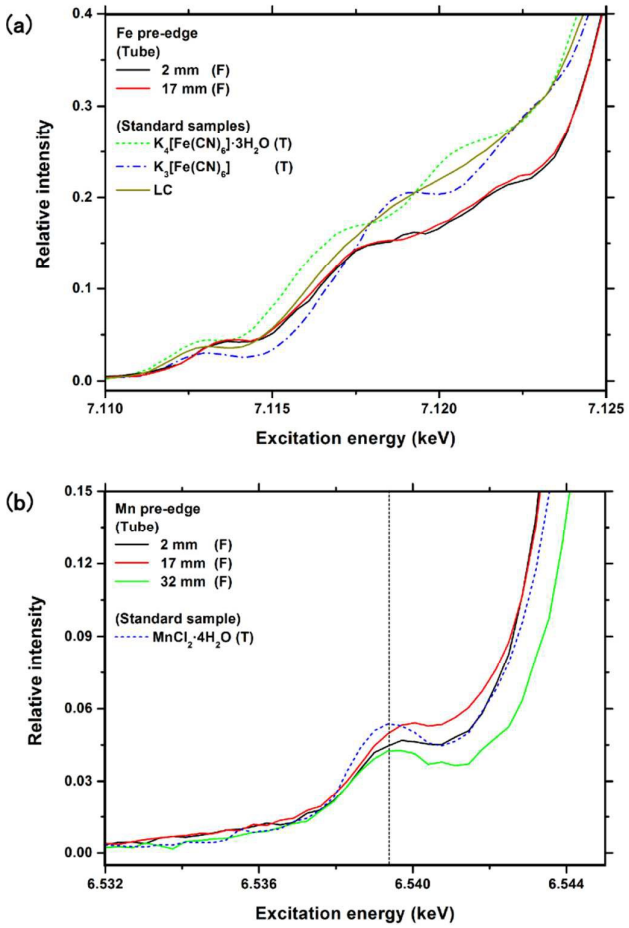

Fig. 7 (a) Fe pre-edge spectra of the sample tube, $K_4[Fe(CN)_6]\cdot 3H_2O$, and $K_3[Fe(CN)_6]$, and (b) Mn pre-edge spectra of the sample tube and $MnCl_2\cdot 4H_2O$. The linear combination of the $K_4[Fe(CN)_6]\cdot 3H_2O$ and $K_3[Fe(CN)_6]$ spectra is shown as "LC" (a). The vertical dotted line serves as a guide to the eye.

In Fig. 7(a) and 7(b), the pre-edge profiles observed below 7.125 keV in Fig. 6(a) and 6.545 keV in 6(b) are re-plotted on an expanded scale. The profiles of $K_4[Fe(CN)_6]\cdot 3H_2O$, $K_3[Fe(CN)_6]$, and $MnCl_2\cdot 4H_2O$ agree with those reported in refs. 60 ($K_4[Fe(CN)_6]\cdot 3H_2O$ and $K_3[Fe(CN)_6]$) and 61 ($MnBr_2\cdot 4H_2O$, the analog of $MnCl_2\cdot 4H_2O$). Possible fine structure in the pre-edge spectra[62] is thought to be smeared out by the instrumental resolution (~1.4 eV).

In contrast to the main-edge profiles [Fig. 6(a)], the pre-edge profiles of $K_4[Fe(CN)_6]\cdot 3H_2O$ and $K_3[Fe(CN)_6]$ [Fig. 7(a)] differ from each other and depend on the Fe oxidation state.[34] Meanwhile, the sample tube spectra are almost identical indicating the same Fe oxidation state at the two positions. These spectra are represented as a linear combination (LC) of the two standard samples by trial and error. The "LC" in Fig. 7(a) is the best-fit result, where the ratio of $K_4[Fe(CN)_6]\cdot 3H_2O$ to $K_3[Fe(CN)_6]$ is 1:1. The LC profile reproduced the overall shape of the sample tube spectra, suggesting that the Fe oxidation state in the sample tube lies between 2+ and 3+. However, in the high-energy region (>~7.117 keV), the LC overestimated the sample tube intensity by ~25%. The origin of the low intensity of the sample tube spectra is currently unclear, although the change of unoccupied states by the formation of Mn−Fe based PBAs is a possible cause.

The Mn pre-edge spectra of the sample tube differ from one another and from the $MnCl_2\cdot 4H_2O$ spectrum, in correspondence with the differences in the Mn main-edge spectra [Fig. 6(b)]. However, all Mn spectra have a common peak-like feature at 6.539 keV of weak intensity [compare the vertical axes of Fig. 7(a) and (b)]. The weak 6.539 keV feature is assigned to forbidden Mn 1s → Mn 3d transitions, and is characteristic of Mn^{2+} compounds with distorted octahedral coordination environments.[61, 63] This result suggests that the octahedral Mn^{2+} species are predominant in the sample tube.

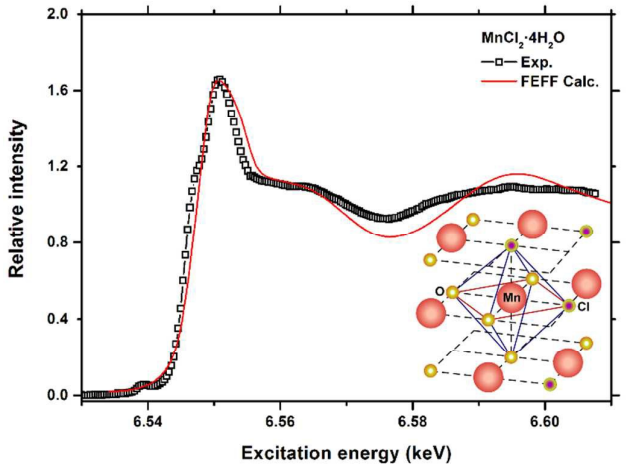

Fig. 8 Mn *K*-edge XANES profile obtained by FEFF calculations for a $[Mn_7O_8Cl_4]$ cluster ("FEFF Calc"). The profile was compared with the experimental Mn *K*-edge XANES spectrum ("Exp"). Inset: A schematic depiction of the employed $[Mn_7O_8Cl_4]$ cluster.

FEFF simulation of XANES spectra

FEFF simulations were conducted to provide a greater understanding of the XANES spectra of the sample tube. For FEFF calculations, we employed a distorted octahedral cluster with a Mn/Fe atom at the center and bond angles fixed at 90°. The maximum value for overlapping muffin tins and the cluster radius for full multiple scattering were 0.10 and 0.65 nm, respectively.

Fig. 8 shows Mn *K*-edge XANES profiles computed by FEFF ("FEFF Calc") for the $[Mn_7O_8Cl_4]$ cluster depicted schematically in the inset. This cluster model was based on the assumption that and the Mn–Cl and Mn–O bond distances are 0.249 and 0.220 nm, respectively.[54] In Fig. 8, the experimental XANES spectrum of $MnCl_2\cdot 4H_2O$ ("Exp") also has been plotted. The theoretical profile reproduced the experimental $MnCl_2\cdot 4H_2O$ spectrum. This finding confirmed that FEFF simulations can be used for quantitative analysis of Mn *K*-edge XANES spectra.

The features in the high-energy region (> ~6.57 keV) of the experimental spectrum are noticeably broader than those of the calculated profile. This points to a disorder in the first shell on the crystal. In fact, the $MnCl_2\cdot 4H_2O$ octahedron is significantly distorted,[64] and the Mn−Cl (0.2475−0.2500 nm) and Mn−O bond length (0.2185−0.2224 nm) and bond angles (87−96°) deviate considerably from the average values employed. Thus, the comparison in Fig. 8 suggests also that Mn *K*-edge XANES can stand for more detailed theoretical studies in future.

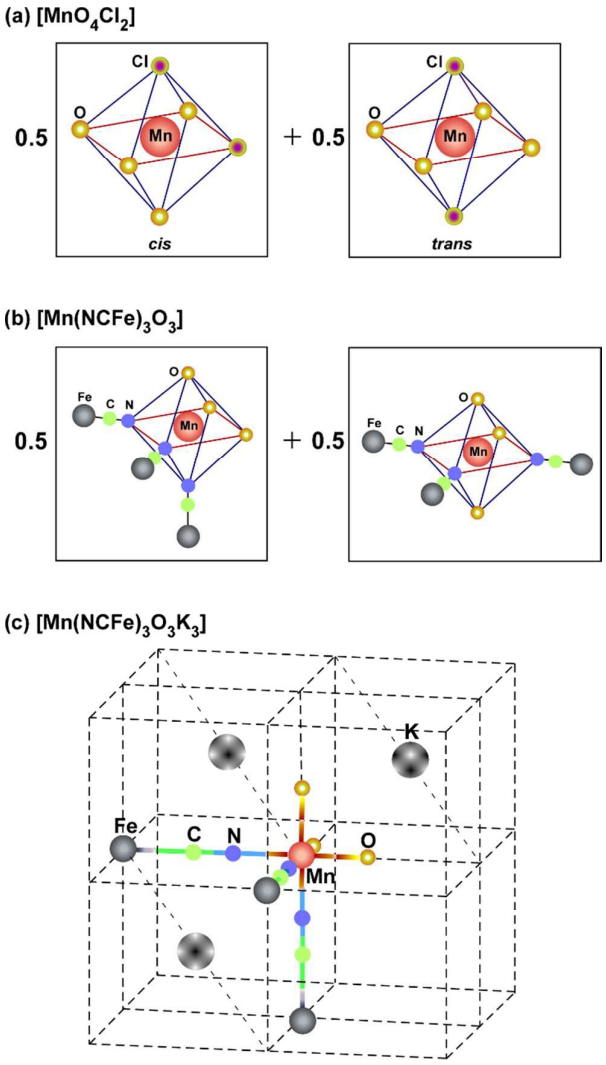

Fig. 9 Schematic depiction of (a) $[MnO_4Cl_2]$, (b) $[Mn(NCFe)_3O_3]$, and (c) $[Mn(NCFe)_3O_3K_3]$ clusters.

To analyze the Mn XANES profiles of the sample tube, we conducted FEFF calculations using several model clusters, the bond distances of which are collected in Table 1. The "MnO_6-1" and "MnO_6-2" clusters have O_h symmetry and were the models for $MnCl_2$ in dilute aqueous solutions.[53,54] The Mn–O bond length of MnO_6-1 was taken from ref. 53; that of MnO_6-2 (0.228 nm) was the best-fit value from the Mn XANES spectrum of the sample tube at 32 mm, as discussed later. The "MnO_5Cl" cluster containing one Cl atom used the best-fit value for the Mn–O bond length and the Mn–Cl bond length from ref. 53. The "MnO_4Cl_2-1" and "MnO_4Cl_2-2" clusters have two Cl atoms, for which *cis* and *trans* geometries are possible. In the current study, the contributions from the two geometries were averaged, as shown schematically in Fig. 9(a). These clusters were the models for concentrated $MnCl_2$ solutions.[53,54] While the Mn–Cl bond length for the two clusters was taken from ref. 53, different Mn–O bond lengths were employed. The ref. 53 value was used for MnO_4Cl_2-1, and the best-fit value was used for MnO_4Cl_2-2.

The "$Mn(NCFe)_6$-1," "$Mn(NCFe)_6$-2," "$Mn(NCFe)_6$-3," "$Mn(NCFe)_5O$," "$Mn(NCFe)_3O_3$," "$Mn(NCFe)_3O_3K_3$," and "$Mn(NCFe)_3O_3K_4$" were model clusters for several types of Mn−Fe-based PBAs. $Mn(NCFe)_6$-1, $Mn(NCFe)_6$-2, and $Mn(NCFe)_6$-3 modeled a PBA with a Mn atom surrounded by six $[Fe(CN)_6]$ groups. The 0.221-nm Mn–N bond length of $Mn(NCFe)_6$-1 was obtained from the result reported for $RbMn[Fe(CN)_6].H_2O$.[41] For comparison, the Mn–N bond lengths of $Mn(NCFe)_6$-2 and $Mn(NCFe)_6$-3 deviated from 0.221 nm by ±0.009 nm. The $Mn(NCFe)_5O$ and $Mn(NCFe)_3O_3$ clusters modeled complexes where the $[Fe(CN)_6]$ moieties were partially replaced by one and three O atoms (conceivably as water molecules), respectively. Two geometries are possible for the $Mn(NCFe)_3O_3$ cluster, as shown in Fig. 9(b). As was the case for MnO_4Cl_2, the contributions from the two geometries were averaged. The $Mn(NCFe)_3O_3K_3$ and $Mn(NCFe)_3O_3K_4$ clusters were models for PBAs wherein three and four K^+ ions, respectively, were inserted in the $Mn(NCFe)_3O_3$-type species. Fig. 9(c) gives a schematic depiction of the $Mn(NCFe)_3O_3K_3$ cluster with the O atoms set at (t, 0, 0), (0, t, 0), and (0, 0, t) (where $t > 0$ is the Mn–O distance) and the K atoms set at (-u, -u, -u), (u, u, u), and (-u, u, -u) (where $0 < u <$ the Mn–Fe distance). In $Mn(NCFe)_3O_3K_4$ cluster, the K atoms were set at (-u, -u, -u), (u, u, -u), (u, -u, u), and (-u, u, u).

The Mn–C and Mn–Fe lengths in Table 1 were obtained by adding the N–C length (0.113 nm in Prussian blue[65]) and the C–Fe length (0.193 nm in $RbMn[Fe(CN)_6].H_2O$[41]) to the above Mn–N length. The Mn–K length of 0.433 nm was the best-fit value for the Mn XANES spectra of the sample tube at 2 mm. As discussed later, two Mn-O distances, the 0.220-nm aqueous solution and 0.228-nm best-fit values, were employed for calculations of the $[Mn(NCFe)_xO_{6-x}K_y]$-type clusters.

Table 1 Bond lengths of the clusters representing sample species

Symbols	Cluster type	Mn–O (nm)	Mn–Cl (nm)	Mn–N (nm)	Mn–C (nm)	Mn–Fe (nm)	Mn–K (nm)
	$[MnO_xCl_{6-x}]$						
MnO_6-1	$[MnO_6]$	0.220	–	–	–	–	–
MnO_6-2	$[MnO_6]$	0.228	–	–	–	–	–
MnO_5Cl	$[MnO_5Cl]$	0.228	0.249	–	–	–	–
MnO_4Cl_2-1	$[MnO_4Cl_2]$	0.220	0.249	–	–	–	–
MnO_4Cl_2-2	$[MnO_4Cl_2]$	0.228	0.249	–	–	–	–
	$[Mn(NCFe)_xO_{6-x}K_y]$						
$Mn(NCFe)_6$-1	$[Mn(NCFe)_6]$	–	–	0.221	0.334	0.527	–
$Mn(NCFe)_6$-2	$[Mn(NCFe)_6]$	–	–	0.212	0.325	0.518	–
$Mn(NCFe)_6$-3	$[Mn(NCFe)_6]$	–	–	0.230	0.343	0.536	–
$Mn(NCFe)_5O$	$[Mn(NCFe)_5O]$	0.220	–	0.221	0.334	0.527	–
$Mn(NCFe)_3O_3$	$[Mn(NCFe)_3O_3]$	0.220	–	0.221	0.334	0.527	–
$Mn(NCFe)_3O_3K_3$	$[Mn(NCFe)_3O_3K_3]$	0.228	–	0.221	0.334	0.527	0.433
$Mn(NCFe)_3O_3K_4$	$[Mn(NCFe)_3O_3K_4]$	0.228	–	0.221	0.334	0.527	0.433

Fig. 10(a) shows Mn *K*-edge XANES profiles computed by FEFF for the MnO_xCl_{6-x} ($x \leq 2$) clusters in Table 1. For comparison, the experimental XANES spectra obtained at 17 and 32 mm also are plotted. Interestingly, XANES profiles calculated from models with the 0.220-nm aqueous solutions Mn–O length (MnO_6-1 and MnO_4Cl_2-1) considerably overestimated the experimental spectra in the region from 6.55 to 6.58 keV. In contrast, profiles using a model with a slightly longer Mn–O length showed better agreement with experimental data. The best-fit Mn–O length value was 0.228 nm, which was employed in the MnO_6-2 cluster. This result strongly suggests that the average Mn–O distance in the sample tube is slightly, but noticeably, longer than that in $MnCl_2$ solutions.

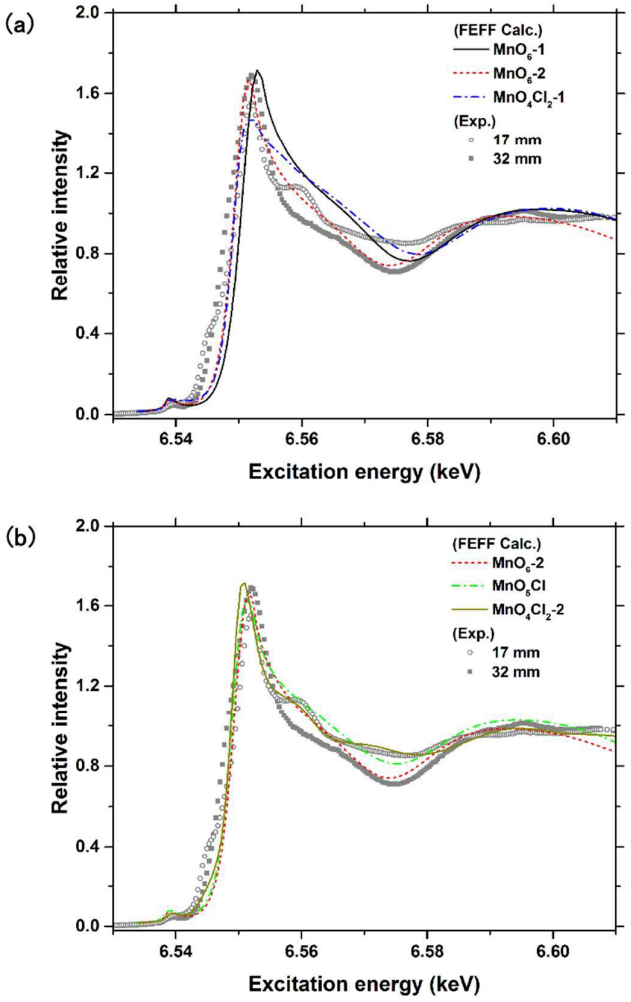

Fig. 10 Mn *K*-edge XANES profiles obtained by FEFF calculations for (a) MnO_6-1, MnO_6-2, and MnO_4Cl_2-1 and (b) MnO_5Cl and MnO_4Cl_2-2 for comparison with the XANES spectra measured at 17 and 32 mm. The MnO_6-2 profile was added in (b) for further comparison.

Fig. 10(b) shows the effects of substituting Cl for O on the XANES profile of MnO_xCl_{6-x} type clusters with the best-fit Mn–O length. Increasing Cl substitution made the valley at ~6.575 keV shallower and produced a slight shift of the white line to the low energy. This change explains in part the differences between the 17-mm and 32-mm XANES spectra and suggests that substitution of O by Cl contributes to the increased intensity at 6.555 to 6.58 keV in the XANES profiles.

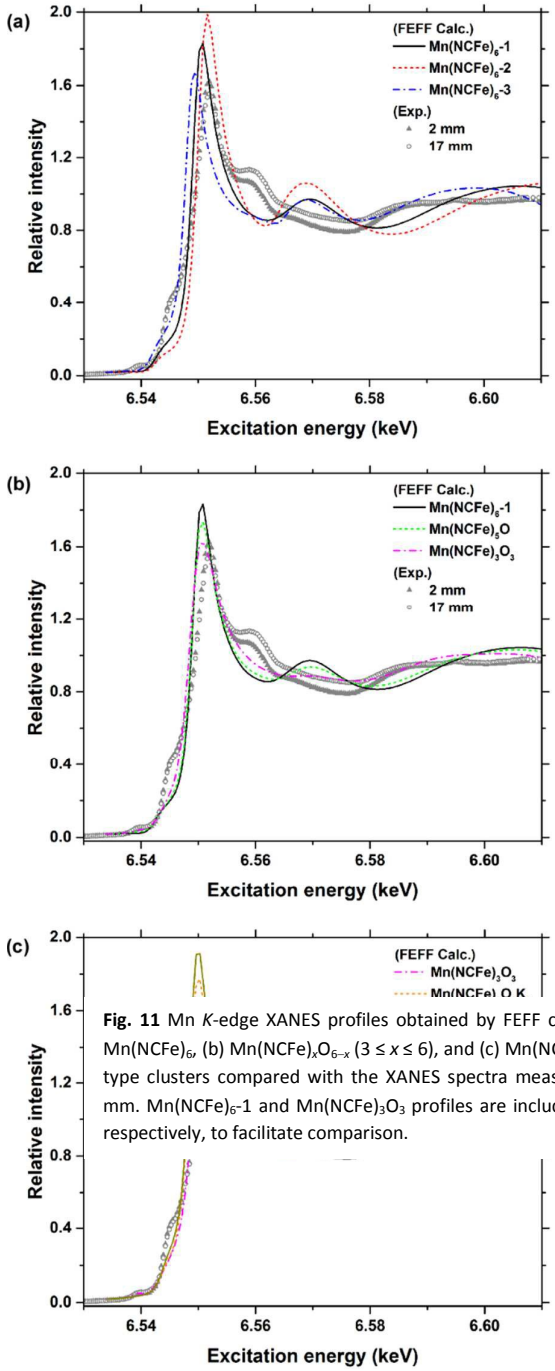

Fig. 11 Mn *K*-edge XANES profiles obtained by FEFF calculations for (a) $Mn(NCFe)_6$, (b) $Mn(NCFe)_xO_{6-x}$ ($3 \leq x \leq 6$), and (c) $Mn(NCFe)_3O_3K_y$ ($y = 3, 4$) type clusters compared with the XANES spectra measured at 2 and 17 mm. $Mn(NCFe)_6$-1 and $Mn(NCFe)_3O_3$ profiles are included in (b) and (c), respectively, to facilitate comparison.

Fig. 11(a) shows Mn *K*-edge XANES profiles computed by FEFF for the [Mn(NCFe)$_6$]-type clusters in Table 1. The calculated profiles show a pronounced effect of Mn−N bond length. An increase in the Mn−N bond length (2→1→3) shifted the white line and the broad third peak to lower energy, but did not influence the position of the second peak at 6.57 keV. This result suggests that the 6.57 keV peak is a characteristic feature of [Mn(NCFe)$_6$]-type species.

For comparison, experimental XANES spectra obtained at 2 and 17 mm also are plotted in Fig. 11(a). No calculation quantitatively reproduced these experimental profiles. In particular, none of the experimental Mn *K*-edge spectra exhibited the 6.57 keV peak (Figs. 6, 10, and 11). Thus, [Mn(NCFe)$_6$]-type species were not predominant in the sample tube: *i.e.*, the Mn−Fe-based PBAs formed in the sample tube have [Fe(CN)$_6$] vacancies.[40] The extent of the [Fe(CN)$_6$] vacancies depends on preparation conditions and determines important properties of PBAs.[40] This topic will be discussed later.

Among the calculated profiles in Fig. 11(a), Mn(NCFe)$_6$-1 provided the most consistent prediction of white line energy and spectral intensity. Thus, we used the 0.221-nm Mn−N bond length of Mn(NCFe)$_6$-1 (from RbMn[Fe(CN)$_6$].H$_2$O[41]) in the following calculations.

Fig. 11(b) shows Mn *K*-edge XANES profiles for the Mn(NCFe)$_x$O$_{6-x}$ ($3 \leq x \leq 6$) type clusters in Table 1. The calculations indicate that the intensity of the 6.57 keV peak, a characteristic feature of Mn(NCFe)$_6$ clusters, decreases with the increasing substitution of O. Consequently, the XANES profile shows only a trace of the 6.57 keV peak for Mn(NCFe)$_3$O$_3$.

Comparison of the calculated and experimental XANES spectra in Fig. 11(b) shows that the Mn(NCFe)$_3$O$_3$ profile reproduced the overall experimental XANES spectra, except for the shoulder at 6.56 keV. The profile calculated for Mn(NCFe)$_3$O$_3$K$_y$ clusters in Fig. 11(c) imply that K^+ ions inserted in Mn−Fe-based PBAs [Fig. 9(c)] are the origin of the 6.56 keV shoulder. Fig. 11(c) also shows that calculated Mn(NCFe)$_3$O$_3$K$_y$ profiles do not perfectly reproduce the experimental spectra. For example, experimental intensities are underestimated by the calculated profiles from ~6.55 to 6.57 keV, and the white line are shifted to the lower energy with marked overestimates of intensity. These results suggest that [Mn(NCFe)$_3$O$_3$K$_y$]-type species exist at 2 and 17 mm in the sample tube, but in the presence of other chemical species.

In Fig. 12, Mn *K*-edge XANES spectra measured at (a) 32, (b) 17, and (c) 2 mm in the sample tube are compared with calculated profiles. As shown in Fig. 10, the 32-mm XANES was in good qualitative agreement with the MnO$_6$-2 calculation, but not with those of MnO$_4$Cl$_2$-2 and Mn(NCFe)$_3$O$_3$K$_3$. In addition, the 6.57 keV peak and 6.56 keV shoulder were missing. These results mean that Mn−Fe-based PBAs were exiguous in the sparse band region at 32 mm and that MnO$_6$ species (the outer electrolyte analogs) were predominant, although brown Liesegang bands were observed macroscopically.

XANES spectra measured at 17 and 2 mm contain a shoulder at 6.56 keV, which indicates the presence of Mn−Fe-based PBAs (Mn(NCFe)$_x$O$_{6-x}$K$_y$) at these positions in the sample tube. These spectra were analyzed further by a trial and

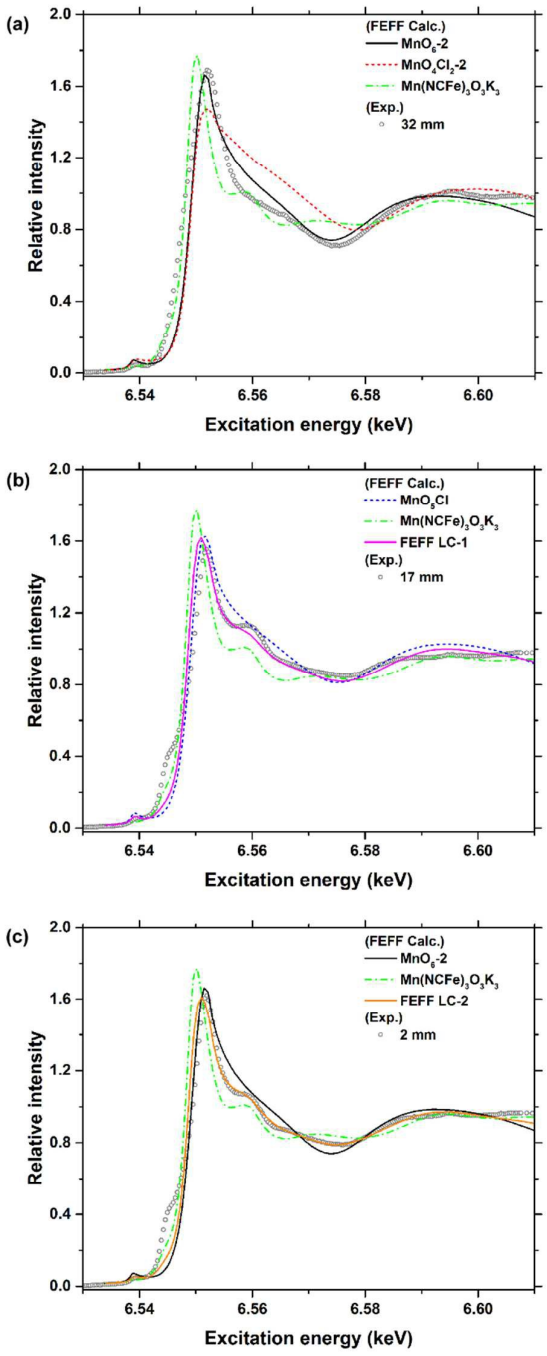

Fig. 12 Comparisons of Mn *K*-edge XANES spectra measured at (a) 32, (b) 17, and (c) 2 mm with the FEFF calculations. The linear combinations of the calculated profiles, "FEFF LC-1" and "FEFF LC-2," are shown in (b) and (c), respectively.

error linear combination of calculated profiles.

"FEFF LC-1" in Fig. 12(b), which consists of 0.60 MnO$_5$Cl plus 0.40 Mn(NCFe)$_3$O$_3$K$_3$, provided the best-fit result for the

17-mm spectrum and gave good agreement for the white line and the following shallow valley. This suggests that in the dense band region of the sample tube (17 mm), $[Mn(NCFe)_3O_3K_3]$-type PBAs coexist as minor components with MnO_5Cl species (partially Cl-substituted outer electrolyte analogs).

"FEFF-LC 2" in Fig. 12(c), which consists of 0.50 MnO_6-2 plus 0.50 $Mn(NCFe)_3O_3K_3$, provides the best-fit result and a quantitative reproduction of the 2-mm XANES spectrum. This result strongly suggests that the 2-mm turbid zone of the sample tube contains a high concentration of $[Mn(NCFe)_3O_3K_3]$-type PBAs in the presence of MnO_6 species.

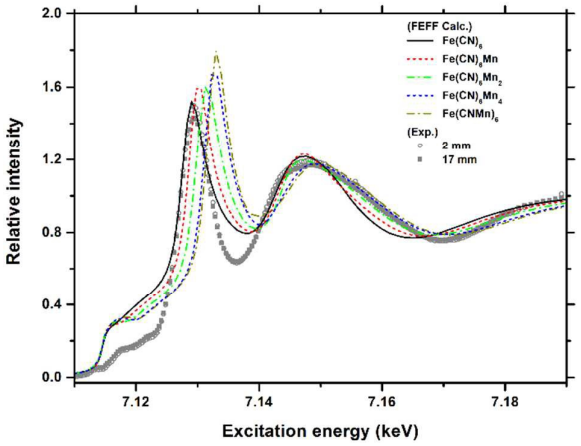

Fig. 13 Fe *K*-edge XANES profiles obtained by FEFF calculations for $Fe(CN)_6$, $Fe(CN)_6Mn$, $Fe(CN)_6Mn_2$, $Fe(CN)_6Mn_4$, and $Fe(CNMn)_6$ clusters compared with XANES spectra measured at 2 and 17 mm.

To assess the results obtained from the Mn XANES analysis, we also computed Fe *K*-edge XANES profiles by FEFF using the $Mn(NCFe)_6$-1 bond lengths in Table 1. Fig. 13 shows the Fe *K*-edge XANES profiles calculated for "$Fe(CN)_6$," "$Fe(CN)_6Mn$," "$Fe(CN)_6Mn_2$," "$Fe(CN)_6Mn_4$," and "$Fe(CNMn)_6$." Here, the $Fe(CN)_6$ cluster modeled a "free" $[Fe(CN)_6]$ ion, where no Mn ion is connected. $Fe(CN)_6Mn$, $Fe(CN)_6Mn_2$, $Fe(CN)_6Mn_4$, and $Fe(CNMn)_6$ modeled Mn−Fe-based PBA with one, two, four, and six Mn−N bonds, respectively. In $Fe(CN)_6Mn_2$ and $Fe(CN)_6Mn_4$, the contributions from *cis* and *trans* geometries were averaged.

Although the pre-edge intensity was largely overestimated, and the depth of the 7.136 keV valley and width of the second band were underestimated, the $Fe(CN)_6$ profile almost perfectly predicted the peak energies of all bands (Fig. 13). This result confirmed the validity of the bond lengths used for Mn XANES analysis (Mn−Fe: 0.527 nm, Mn−C: 0.334 nm, and Mn−N: 0.221 nm). The underestimation of the valley depth and band width indicates that more detailed cluster models are needed to better reproduce the experimental data. The disagreement in the pre-edge region, which also was found in the Mn *K*-edge XANES analysis (Fig. 12), will be discussed later.

The $Fe(CN)_6Mn$, $Fe(CN)_6Mn_2$, $Fe(CN)_6Mn_4$, and $Fe(CNMn)_6$ profiles indicate that an increase in the number of coordinated Mn atoms shifts the white line peak to higher energy and broadens the second band. Consequently, discrepancies between experimental and calculated data become large for clusters such as $Fe(CNMn)_6$ with a large number of Mn atoms. This suggests that $[Fe(CN)_6]$ ions in the sample tube are less connected to Mn^{2+} ions, supporting that Mn−Fe-based PBAs, in particular, $[Mn(NCFe)_6]$-type species are minor components in the sample tube.

In the pre-edge region, both Mn (Fig. 12) and Fe *K*-edge XANES calculations (Fig. 13) show some disagreement with experimental spectra. Possible reasons for pre-edge discrepancies include the following. Firstly, because the *K* pre-edge spectra of 3d elements are (at least, partially) influenced by 1s→3d quadrupole transitions,[60, 62] dipole-allowed calculations such as FEFF generally give less accurate results. Secondly, the pre-edge region is sensitive to artifacts in FEFF calculations such as the overlap of muffin tins and the radius of clusters in full multiple scattering. FEFF pre-edge profiles can be distorted by these effects. More accurate XANES calculations overcoming these difficulties are a worthwhile future objective.

From the FEFF analysis described above, it is concluded that (1) changes in Mn−Fe-based PBAs concentrations are related to the position dependence of the Mn *K*-edge XANES spectra and (2) Mn−Fe-based PBAs are not major components in the sample tube and do not have the $[Mn(NCFe)_6]$-type local structures.

Conclusion (2) above might disappoint material scientists, because predominance of the $Mn(NCFe)_6$ structure (*i.e.*, fewer $[Fe(CN)_6]$ vacancies) is important in practical applications of PBAs, such as magnets[40] and ion batteries.[45] However, we emphasize that sample preparation was not optimized for $Mn(NCFe)_6$-rich Liesegang pattern formation. In fact, we are in an early stage in our study of PBA pattern formation. There are many factors that can alter Liesegang patterns including experimental geometry,[25] the concentrations of inner and outer electrolytes,[2–5,12,26,27,29,31,52] gel types,[5,12,30,52] gel concentration,[25,29,30] the degree of cross-linking in the gel,[12,52] gel charge,[5,52] pH,[14] co-existing ions,[14,24,26,52] light irradiation,[5,21] and application of an electric field.[25,66,67] Thus, there is room for improving the preparation of $Mn(NCFe)_6$-rich Liesegang patterns. Note also that high-quality single crystals of PBAs generally are prepared under slow-diffusion conditions.[40,41] Introduction of gels into systems that form Liesegang patterns is an option for producing slow diffusions.[5]

The position dependence of the PBA concentration in the tube may be helpful in selecting PBAs with better qualities, even if the PBA Liesegang pattern itself is not useful in microfabrication. The 6.57 keV peak in the Mn XANES spectra will be a good probe for such selections.

Conclusions

Periodic brown bands formed in water-glass gels that were prepared by admixture of 0.15−0.30 M $[Fe(CN)_6]^{3-}$ solutions and 0.53 M acetic acid and contacted by agar gels mixed with 0.15−0.30 M Mn^{2+} solutions. X-ray spectroscopic analyses were conducted on a sample tube prepared from an agar gel

mixed with 0.20 M $MnCl_2$ solution and a water-glass gel mixed with 0.25 M $K_3[Fe(CN)_6]$ solution. Periodic patterns in the sample tube obeyed an empirical set of scaling laws, showed no marked second-band effects, and were considered as a Liesegang pattern basically formed by a pre-nucleation mechanism.

Time-resolved XRF measurements indicated that the turbid zone in the sample tube contained diffusive Mn and Fe compounds accumulated from the surroundings. The periodic bands were formed under conditions of low Mn and/or Fe concentration and co-existed with large amounts of unreacted Fe species in the intermediate stage. Furthermore, XRF results indicated that the Mn and Fe concentrations in the turbid zone were 3−6 times greater than in the periodic bands. Thus, Mn−Fe-based PBAs were produced primarily in the turbid zone and contributed to the formation of a Liesegang pattern in the lower region.

Position-dependent XANES measurements indicated that the Fe local structure in the sample tube was almost independent of the measuring point and consisted primarily of $[Fe(CN)_6]$. In contrast, the Mn local structure depended significantly on positions. FEFF cluster calculations suggested that (1) Mn−Fe-based PBAs co-exist with $[MnO_6]$ or $[MnO_5Cl]$ species, (2) their compositions varies with the position of measurement, and (3) the most likely Mn local structure of the predominant PBAs is $[Mn(NCFe)_3O_3K_3]$.

The combination of time-resolved XRF and position-dependent XANES is demonstrated to be a powerful tool for analyzing the Liesegang patterning stemming from the formation of PBAs, which are not fully under-stood but are potentially useful in material science.

Acknowledgments

The authors are grateful to Ms. M. Katakura, Ms. E. Hashimoto, and Ms. E. Kiriya of Japan Women's University for their help in sample preparation and data treatment. The XANES experiments at KEK-PF were conducted under proposal No. 2014G505. This study was supported by JSPS KAKENHI Grant Number 26410163 and Number 24710102.

References

1. D. Feinn, P. Ortoleva, W. Scalf, S. Schmidt and M. Wolf, *J. Chem. Phys.,* 1978, ***69***, 27.
2. S. Kai, S. C. Müller and J. Ross, *J. Chem. Phys.,* 1982, **76**, 1392.
3. S. C. Müller, S. Kai and J. Ross, *J. Phys. Chem.,* 1982, **86**, 4078.
4. S. Kai, S. C. Müller and J. Ross, *J. Phys. Chem.,* 1983, **87**, 806.
5. H. Henisch, *Crystals in Gels and Liesegang Rings*, Cambridge University Press, Cambridge, 1988.
6. H.-J. Krug and H. Brandtstädter, *J. Phys. Chem. A,* 1999, **103**, 7811.
7. D. Xie, J. Wu, G. Xu, Q. Ouyang, R. D. Soloway and T. Hu, *J. Phys. Chem. B,* 1999, **103**, 8602.
8. C. Rodriguez-Navarro, O. Cazalla, K. Elert and E. Sebastian, *Proc. R. Soc. Lond. A,* 2002, **458**, 2261.
9. B. P. J. de Lacy Costello, P. Hantz and N. M. Ratcliffe, *J. Chem. Phys.,* 2004, **120**, 2413.
10. D. A. Stone and R. E. Goldstein, *Proc. Natl. Acad. Sci. USA,* 2004, **101**, 11537.
11. A. Volford, F. Izsák, M. Ripszám and I. Lagzi, *Langmuir,* 2007, **23**, 961.
12. B. A. Grzybowski, *Chemistry in Motion: Reaction−Diffusion Systems for Micro- and Nanotechnology*, John Wiley & Sons, Chichester, 2009.
13. L. Qi, *Coord. Chem. Rev.,* 2010, **254**, 1054.
14. I. Lagzi, *Precipitation Patterns in Reaction−Diffusion Systems*, ed. I. Lagzi, Research Signpost, Kerala, India, 2010.
15. T. Karam, H. El-Rassy, V. Nasreddine, F. Zaknoun, S. El-Joubeily, A. Z. Eddin, H. Farah, J. Husami, S. Isber and R. Sultan, *Chaotic Model. Simul.,* 2013, **3**, 451.
16. B. A. Grzybowski, K. J. M. Bishop, C. J. Campbell, M. Fialkowski and S. K. Smoukov, *Soft Matter*, 2005, **1**, 114.
17. B. A. Grzybowski and C. J. Campbell, *Mater. Today*, 2007, **10**, 38.
18. C. Wagner, *J. Collid. Sci.,* 1950, **5**, 85.
19. M. Flicker and J. Ross, *J. Chem. Phys.,* 1974, **60**, 3458.
20. G. T. Dee, *Phys. Rev. Lett.,* 1986, **57**, 275.
21. I. Das, A. Pushkarna and N. R. Agrawal, *J. Phys. Chem.,* 1989, **93**, 7269.
22. Z. Rácz, *Physica A,* 1999, **274**, 50.
23. M. Chacron and I. L'Heureux, *Phys. Lett. A,* 1999, **263**, 70.
24. L. Mandalian, M. Fahs, M. Al-Ghoul and R. Sultan, *J. Phys. Chem. B*, 2004, **108**, 1507.
25. Z. Shreif, L. Mandalian, A. Abi-Haydar and R. Sultan, *Phys. Chem. Chem. Phys.*, 2004, **6**, 3461.
26. M. Msharrafieh, M. Al-Ghoul, H. Batlouni and R. Sultan, *J. Phys. Chem. A*, 2007, **111**, 6967.
27. M. Al-Ghoul, T. Ghaddar and T. Moukalled, *J. Phys. Chem. B*, 2009, **113**, 11594.
28. I. Lagzi, B. Kowalczyk and B. A. Grzybowski, *J. Am. Chem. Soc.*, 2010, **132**, 58.
29. T. Karam, H. El-Rassy and R. Sultan, *J. Phys. Chem. A*, 2011, **115**, 2994.
30. I. Lagzi, *Langmuir*, 2012, **28**, 3350.
31. M. Al-Ghoul, M. Ammar and R. O. Al-Kaysi, *J. Phys. Chem. A*, 2012, **116**, 4427.
32. H. Nabika, M. Sato and K. Unoura, *Langmuir*, 2014, **30**, 5047.
33. R. E. Liesegang, *Naturwiss. Wochenschr.*, 1896, **11**, 353.
34. H. Hayashi and H. Abe, *J. Anal. At. Spectrom.,* 2016, **31**, 912.
35. ed. K. Tsuji, J. Injuk and R. Van Grieken, *X-Ray Spectrometry: Recent Technological Advances*, John Wiley & Sons, Chichester, 2004.
36. H. Hayashi, *Chemical Effects in Hard X-ray Photon-In Photon-Out Spectra*, in *Encyclopedia of Analytical Chemistry*, ed. R. A. Meyers, John Wiley & Sons, Chichester, 2014. DOI: 10.1002/9780470027318.a9389.
37. M. West, A. T. Ellis, P. J. Potts, C. Streli, C. Vanhoof and P. Wobrauschek, *J. Anal. At. Spectrom.*, 2015, **30**, 1839.
38. F. de Groot, *Chem. Rev.,* 2001, **101**, 1779.
39. F. de Groot and A. Kotani, *Core Level Spectroscopy of Solids*, CRC Press, Boca Raton, 2008.
40. M. Verdaguer and G. Girolami, *Magnetic Prussian Blue Analogs*, in ed. J. S. Miller and M. Drillon, *Magnetism: Molecules to Materials V.*, Wiley−VCH Verlag GmbH & Co. KGaA, Weinheim, 2004.
41. E. J. M. Vertelman, T. T. A. Lummen, A. Meetsma, M. W. Bouwkamp, G. Molnar, P. H. M. van Loosdrecht and P. J. van Koningsbruggen, *Chem. Mater.,* 2008, **20**, 1236.
42. H. Tokoro, and S. Ohkoshi, *Photo-Induced Phase Transition in RbMnFe Prussian Blue Analog-Based Magnet*, in ed. M. Ohtsu, *Progress in Nano-Electro-Optics VII Chemical, Biological, and Nanophotonic Technologies for Nano-Optical Devices and Systems*, Springer−Verlag, Berlin, 2010.

43. D. M. Pajerowski, J. E. Gardner, F. A. Frye, M. J. Andrus, M. F. Dumont, E. S. Knowles, M. W. Meisel and D. R. Talham, *Chem. Mater.*, 2011, **23**, 3045.
44. A. A. Karyakin, *Electroanalysis*, 2001, **13**, 813.
45. D. Yang, J. Xu, X.-Z. Liao, Y.-S. He, H. Liu, Z.-F. Ma, *Chem. Commun.,* 2014, **50**, 13377.
46. P. Nie, L. Shen, H. Luo, B. Ding, G. Xu, J. Wang and X. Zhang, *J. Mater. Chem. A,* 2014, **2**, 5852.
47. A. L. Lipson, B. Pan, S. H. Lapidus, C. Liao, J. T. Vaughey and B. J. Ingram, *Chem. Mater.,* 2015, **27**, 8442.
48. G. Fornasieri, M. Aouadi, E. Delahaye, P. Beaunier, D. Durand, E. Rivière, P-A. Albouy, F. Brisset and A. Bleuzen, *Materials,* 2012, **5**, 385.
49. H. Hayashi, *X-Ray Spectrom.*, 2014, **43**, 292.
50. A. L. Ankudinov, B. Ravel, J. J. Rehr and S. D. Conradson, *Phys. Rev. B*, 1998, **58**, 7565.
51. A. L. Ankudinov, C. E. Bouldin, J. J. Rehr, J. Sims, H. Hung, *Phys. Rev. B*, 2002, **65**, 104107.
52. B. Qu, Ph.D. Dissertation, University of Toronto, Ontario, Canada, 2012.
53. Y. Tajiri, M. Ichihashi, T. Mibuchi and H. Wakita, *Bull. Chem. Soc. Jpn.,* 1986, **59**, 1155.
54. B. Beagley, C. A. McAuliffe, S. P. B. Smith and E. W. White, *J. Phys.: Condens. Matter,* 1991, **3**, 7919.
55. G. Zschornack, *Handbook of X-Ray Data*; Springer–Verlag, Berlin, 2007.
56. R. Jenkins, *An introduction to X-ray spectrometry*, Heyden & Sons, London, 1976.
57. A. Bianconi, M. Dell' Ariccia, P. J. Durham and J. B. Pendry, *Phys. Rev. B*, 1982, **26**, 6502.
58. A. Ohta, H. Tsuno, H. Kagi, Y. Kanai, M. Nomura, R. Zhang, S. Terashima and N. Imai, *Geochem. J.,* 2006, **40**, 363.
59. D. R. Fernando, T. Mizuno, I. E. Woodrow, A. J. M. Baker and R. N. Collins, *New Phytol.,* 2010, **188**, 1014.
60. T. E. Westre, P. Kennepohl, J. G. DeWitt, B. Hedman, K. O. Hodgson and E. I. Solomon, *J. Am. Chem. Soc.*, 1997, **119**, 6297.
61. Y. Chen, J. L. Fulton and W. Partenheimer, *J. Solution Chem.*, 2005, **34**, 993.
62. F. de Groot, G. Vankó and P. Glatzel, *J. Phys.: Condens. Matter*, 2009, **21**, 104207.
63. M. Belli, A. Scafati, A. Bianconi, S. Mobilio, L. Palladino, A. Reale and E. Burattini, *Solid State Commun.*, 1980, **35**, 355.
64. A. Zalkin, J. D. Forrester and D. H. Templeton, *Inorg. Chem.*, 1964, **3**, 529.
65. P. Glatzel, L. Jacquamet, U. Bergmann, F. M. F. de Groot and S. P. Cramer, *Inorg. Chem.*, 2002, **41**, 3121.
66. I. Das, A. Pushkarna and S. Chand, *J. Colloid Interf. Sci.,* 1992, **150**, 178.
67. I. Bena, M. Droz, I. Lagzi, K. Martens, Z. Rácz and A. Volford, *Phys. Rev. Lett.*, 2008, **101**, 075701.